6

3D Optical Imaging of Fluorescent Agents in Biological Tissues

Manuel Freiberger and Hermann Scharfetter
Graz University of Technology
Austria

1. Introduction

Fluorescence diffuse optical tomography (fDOT) is an imaging modality which goes beyond well-established techniques such as 2D fluorescence imaging and fluorescence microscopy. Being a 3D tomographic modality, it seeks to overcome limitations of 2D systems as are: (i) the determination of the depth of fluorescent objects and (ii) a correction of the broadening of the fluorescence signal due to the massive scattering of photons.

Compared to high-resolution tomography systems such as CT and MRI, fDOT has the particular advantage that the optical activity of many fluorophores is influenced by the chemical milieu in which they are located and, thus, by the biological surrounding. Researchers have already shown the dependency on the oxygenation of the tissue (Longmuir & Knopp (1976); Shives et al. (2002)), the pH value (Gannot et al. (2004); Mordon et al. (1992)), or the temperature (Chen & Wood (2009)), for example. This influence on metabolic processes and states offers information beyond the visualization of anatomical structures and, therefore, is termed *functional imaging*.

In comparison to 2D in-vivo imaging, 3D sensing of fluorescent particles in biological specimen imposes additional problems:

- Light of lower wavelength (blue and green) is absorbed by many biologically relevant materials such as hemoglobin. In order to excite deep fluorophore-structures, excitation light in the far red and near infrared (NIR) range has to be used, which requires suitable (i.e. NIR-excitable) fluorescent targets.
- Visible and NIR-light is heavily scattered in biological tissue. This compromises the achievable resolution especially in comparison to CT and MR and requires special treatment during image reconstruction.
- The light intensity decays exponentially with the probing depth, which infers a depth-dependent maximum resolution.

The outline of this chapter is as follows: In section 2 the optical properties of tissue will be introduced. Section 3 deals with possible hardware setups for 3D sensing. Mathematical models for light propagation are described in section 4. In section 5 nonlinear image reconstruction methods are compared. An overview about clinical and pre-clinical applications is given in section 6 and section 7 concludes with an outlook.

2. Optical properties of tissue

For the determination of the 3D distribution of fluorescent particles inside biological samples, it is necessary to describe light propagation in tissue with mathematical models. This in turn requires to quantify typical light-tissue interaction processes in terms of measurable quantities. The most common processes are certainly absorption and scattering of photons as well as fluorescence and phosphorescence phenomena.

2.1 Absorption

Absorption is the extinction of a photon, whose energy is stored by the absorbing medium via excitation of an electron or in rotational or vibrational states of atoms. This physical processes are stochastic in their nature and therefore should be described by a probability density measure. However, for most models it is sufficient to give the average occurrence rate of an absorption event per photon path length. This leads to the definition of the absorption coefficient μ_a given in units of inverse length; frequently in cm^{-1} or mm^{-1}. It specifies the average number of photons being absorbed when traveling a given distance inside an absorbing medium. An absorption coefficient of $0.2\,\mathrm{cm}^{-1}$ would mean an average of two absorption events per 10 cm which the photon travels inside the object. In other words, a photon can on average travel μ_a^{-1} ($= 5\,\mathrm{cm}$ for the former example) without being absorbed. The latter quantity is called the *mean absorption-free path length*.

2.2 Scattering

Scattering is the deflection of a photon out of its original trajectory into a new direction. In analogy to absorption, the scattering coefficient μ_s gives the average number of scattering events per length of travel. The inverse μ_s^{-1} is the average length a photon can propagate in tissue without being scattered and is thus known as *mean scattering-free path length*. To fully quantify the scattering behavior of some medium, it is not sufficient to know only how often scattering happens but also the direction into which the photon will be deflected is of importance. The latter is given by the scattering phase function $\Theta(\hat{s}, \hat{s}')$, which is the probability for a photon arriving from direction $\hat{s}$ to be scattered into a new direction $\hat{s}'$. Two possible scattering phase functions are depicted in Figure 1. If every scattered direction $\hat{s}'$ has the same probability, the scattering is said to be *isotropic*. This ideal case is not valid in biological media, where scattering is usually strongly forward biased as displayed on the right in Figure 1. At this point, it is also worth noticing that most tissue types are much more scattering than absorbing. Exceptions to this rule are well perfused tissues such as liver and highly transparent liquids as liquor, for example.

2.3 Scattering anisotropy factor

For many real-world applications the description of the scattering distribution by the scattering phase function is much too complicated to be useful. Instead, one seeks to approximate the anisotropic scattering with a scattering coefficient μ_s through an isotropic model with another scattering coefficient μ_s'. To this end, the scattering anisotropy factor g is introduced which is the mean value of the cosine of the scattering angle. This factor is in the range from -1 to 1. Positive values indicate a preference for forward-scattering while negative values indicate an imbalance towards photons which are back-scattered. In the isotropic case g is equal to 0.

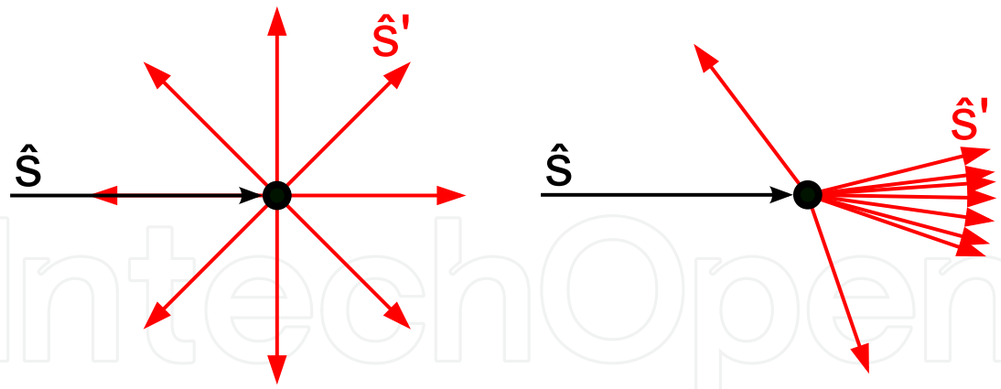

Fig. 1. Visualization of two scattering phase functions. The incoming photons with direction $\hat{s}$ are drawn in black, the scattered ones having a direction $\hat{s}'$ in red. Left: The scattering angles are equally distributed; the scattering is isotropic. Right: Nearly all photons are scattered in a forward direction which is true for most biological tissues.

With the definition of the anisotropy coefficient, one can define the reduced scattering coefficient μ_s' as $\mu_s' := (1-g)\mu_s$. The idea is to approximate anisotropic (forward-directed) scattering with probability μ_s and anisotropy g by isotropic scattering with a smaller scattering coefficient μ_s'. This working principle is illustrated in Figure 2. The true path of a scattered photon is sketched with small arrows. If the anisotropy coefficient of the tissue was $g = 0.875$, every $(1-0.875)^{-1} = 8$ anisotropic steps would be combined into one isotropic step. Thus, the number of scattering events per length of travel decreases and the mean scattering-free path length increases. The approximated scattering can be assumed to be isotropic.

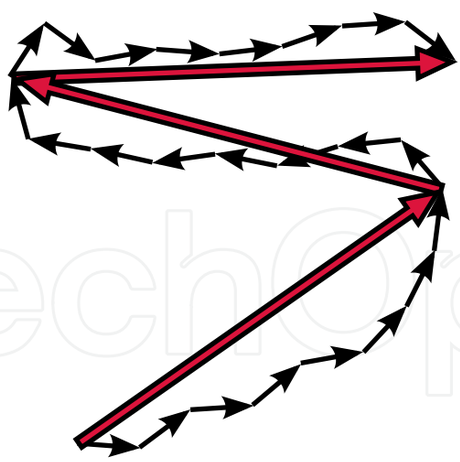

Fig. 2. Principle of the anisotropy coefficient: The short arrows represent the path of a scattered photon in tissue. Each arrow is of length μ_s^{-1}, which is the mean scattering-free path length. Assuming $g = 0.875$, every eight anisotropic scattering events are approximated by one isotropic scattering event which is drawn with red arrows. The isotropic scattering has a reduced scattering coefficient $\mu_s' = (1-g)\mu_s$, i.e. the isotropic mean scattering-free path length is larger than the anisotropic one.

2.4 Diagnostic window

The tissue's ability to absorb photons is a highly wavelength-dependent property. In the so called *diagnostic window* around 650–1300 nm, most tissues are sufficiently weak absorbers and light can penetrate deepest. The lower wavelength boundary of this wavelength range is made up by oxygenated and de-oxygenated hemoglobin; the upper boundary is due to the absorption of water.

3. Hardware

Since the early days of fDOT a number of different systems has been built, most of them for research purposes, but meanwhile also commercial systems are available. Regarding the details of implementation the systems differ considerably, for a good review see e.g. Leblond et al. (2010). A basic distinction can be made concerning the operation mode in terms of its temporal behavior. For some applications the reconstruction of intensity images is sufficient and then the system can operate in continuous-wave (CW) mode, thus leading to CW fluorescence tomography (CWFT). If, however, also the fluorescence lifetime ought to be imaged, the response of the sample to either very short light pulses (usually shorter than 100 ps) or harmonically modulated light with modulation frequencies between several tens of MHz up to several GHz must be acquired. The respective technologies are termed *time domain fluorescence tomography* (TDFT) or *frequency domain fluorescence tomography* (FDFT). All three modes can also be used spectroscopically, which requires in addition a dispersive element or a tunable filter at the detector side.

While the idea of TDFT is intuitively clear (direct measurement of the decay of the light signal), FDFT is more indirect. It relies on the fact that the complete time domain information can be recovered from quasi-stationary measurements with sinusoidally modulated light at many modulation frequencies—thus sampling in Fourier space—and transforming back to time domain by an inverse Fourier transform. However, the relevant bandwidth of the time domain signals is up to several GHz (Gibson et al. (2005)) and frequency domain systems allow sufficiently accurate operation only up to approximately 1 GHz (Chance et al. (1998)). Thus, currently the equivalence cannot be exploited from the instrumentation point of view. Typical modulation frequencies range from less than 100 MHz up to little more than 1 GHz (Durduran et al. (2010); Masciotti et al. (2009); Reynolds et al. (1997)). Assuming a mono-exponential fluorescence decay the lifetime can be recovered from measurements at a single frequency because a single exponential is Fourier transformed to a low pass of first order and thus the knowledge of modulus and phase of the light signal is sufficient.

All systems realized so far share three main components: A light source, a sample holder and a light detection system.

3.1 Light sources

The light source can have a wide spectral range (e.g. xenon arc lamps) in combination with filters but narrowband sources like lasers and LEDs are increasingly popular due to their versatility and the relative ease of producing either short pulses or properly modulated light. As for standard tomography the light should be concentrated to different locations on the sample surface, collimated beams are required, which favors the use of lasers. In any case the spectrum of the light source should be matched to the absorption spectrum of the fluorophore, but in the case of e.g. small Stokes shifts the excitation wavelength may be chosen somewhat

below the absorption maximum in order to account for the limited steepness of excitation and emission filters. In order to keep the hardware flexible, usually filter wheels with selectable cutoff wavelengths are provided in case of wideband sources so as to adapt the system to different fluorophores.

For CWFT practically any light source with appropriate power and spectral content can be used. As FDFT typically requires modulation up to several 100 MHz, classical wideband sources require a fast optical shutter (electro-optic or acousto-optic, see e.g. Lakowicz (2006)) but such technologies are increasingly replaced by laser diodes which can be easily modulated up to 1 GHz in a useful power range (typically several tens of mW for in vivo applications). Even wideband sources based on lasers (supercontinuum lasers) and tunable diode lasers with external cavity are now available. The highest demands on the source are posed by TDFT. Currently the short light pulses are typically generated by Ti:sapphire lasers but also diode lasers are available which can deliver sufficiently short pulses (Lakowicz (2006)). Ti:sapphire lasers provide the unique feature of being tunable, see e.g. Kumar et al. (2008), where 150 fs-pulses are generated with a repetition rate of 80 MHz in a tuning range between 750 nm and 850 nm. In the same publication the spectral range could still be extended to 500 nm by the use of a super-continuum source based on a poly-crystalline fiber. The 80 MHz repetition rate is widely used and has also been adopted for pulsed laser diodes, e.g. in Soloviev et al. (2009).

3.2 Detectors

On the detector side also a large variety of different realizations can be found. Again a major difference exists between CWFT, TDFT and FDFT. While there is no special restriction in CW operation, TDFT requires very fast and precise time-gating of the detector or single photon counting and precise time correlation between excitation and detection (so called time correlated single photon counting, TCSPC).

The most sensitive and versatile devices are certainly photomultiplier tubes (PMTs), photomultipliers with microchannel plates (MCP-PMTs) and image intensifiers based on MCPs with either optical readout on a phosphor screen or electrical readout on a multi-anode grid. Though comparatively expensive, all these variants of photomultiplier devices offer wide dynamic range and frequently also single photon counting capabilities thus enabling TDFT with TCSPC. The possible photon counting rate is primarily limited by the recovery time after arrival of one pulse which may last several ns.

Avalanche photodiodes (APDs) are also useful detectors but have some limitations: The aperture is small compared to that of PMTs, therefore yielding poorer light collection properties. As APDs exhibit a long tail in their pulse response special active quenching of the avalanche process is necessary in order to arrive at high counting rates. So called single photon avalanche photodiodes (SPADs) are able to detect single photons and most recently imaging arrays have been developed for time-resolved optical imaging with a time resolution of about 100 ps (Li et al. (2010); Niclass et al. (2004); Pavia et al. (2011)).

A very appealing but somewhat exotic detector is the streak camera which, in principle, is a PMT with an electron deflection stage and a phosphor screen. This allows to distribute narrowly spaced subsequent pulses on the screen and thus provides an unrivaled high effective counting rate. Such devices have been used in some instances for spectrally resolved

TCSPC in phase fluorometers but also to generate tomographic slice images in diffuse optical tomography (Hebden et al. (1997)).

Several research groups (e.g. Nothdurft et al. (2009); Patwardhan & Culver (2008); Soloviev et al. (2009); Zhang & Badea (2009)) are using ultrafast time-gated image intensified CCD cameras (ICCD) which allow to sample photons within 300 ps at repetition rates up to 110 MHz. Such cameras can acquire a sequence of time-delayed frames from which the time spread function can be approximately reconstructed. The time resolution is not as good as with TCSPC but the data quality is sufficient for many applications. As reported by Patwardhan & Culver (2008), the Fourier transform can then provide the equivalent frequency domain data up to modulation frequencies of more than 1 GHz.

The detectors also differ in their spectral sensitivity. While most PMTs have a high quantum efficiency at the shorter wavelengths of the visible spectrum (VIS) and even at UV they perform comparatively poorly in the NIR range, especially above 850 nm. APDs based on silicon technology are typically more sensitive in the NIR range and can be used up to 1100 nm.

Both TDFT and FDFT require special electronics after the detectors. FDFT is less demanding and uses either heterodyne or homodyne demodulation of the radio-frequency (RF) signal which can be achieved with a fast detector (e.g. PMT) and subsequent downmixing in an RF stage (for basic concepts see Chance et al. (1998)). Alternatively, the downmixing can also be accomplished directly in the detector by modulating its gain with the local oscillator frequency. This approach is the method of choice when using image intensifiers with phosphor screen because due to the afterglow they are too slow for transmitting the high frequencies. Gain modulation, however, is easily possible at the photocathode, though precautions have to be made with respect to modulation depth because many photocathodes exhibit significant heating at high frequencies due to ohmic losses. Systems operating with this concept usually apply homodyne demodulation (see e.g. Godavarty et al. (2003); Reynolds et al. (1997); Sevick-Muraca & Rasmussen (2008)). Also slow detectors in combination with an electro-optic or acousto-optic shutter can be thought of, but their poorer modulation characteristics usually precludes the use of this technique.

The design of a TSCPC circuitry is non-trivial and comprises two input stages for the reference light pulse and the sample pulse. The arrival times of the pulses are determined by a so-called constant fraction discriminators (CFD) and then passed to a time to voltage converter which is read out by a subsequent analog/digital converter. Only pulses within a certain peak height window are counted, thus excluding pulses arising from thermal emission and cosmic rays. TSCPC boards are commercially available and nowadays fairly compact, even for multidimensional TSCPC with up to 16 channels at prices in the range of several tens of k$, depending on the specification. The currently fastest commercial boards are specified with useful count rates up to 20 MHz. As in single photon counting the excitation light levels are chosen in a way that no more than 1 % of the excitation pulses lead to a detected photon, the limit is currently posed by the laser pulse repetition rate which is typically 80 MHz. The required count rate is then at least 800 000 per second, thus current TSCPC speed is more than sufficient.

Especially older tomographic systems employ PMTs or PMTs with multiple anodes, (e.g. Schmidt et al. (2000)) and fiber-optic coupling to the specimen. Also fiber-coupling and cameras as detectors was reported (Godavarty et al. (2003)). However, the coupling is

a significant source of systematic errors and thus the trend goes towards so-called free-space systems without any physical contact to the sample (Schulz et al. (2004)). An early hybrid solution was reported by Graves et al. (2003) where only the excitation side was fiber-coupled. Free-space systems can still be based on single PMTs, but the light is then collected via collimators or focusing lenses at a distance of several cm from the object surface (Kepshire et al. (2009)). Most instruments, however, employ cameras together with an external or built-in image intensifier. Due to the large number of pixels available on the camera chip, the number of possible detectors is much higher than in PMT-based systems and hence the information content in the data is enhanced.

3.3 Sample holder/manipulation stages

Steering of the light beam can be achieved in different ways. The most common ones are galvanometer-controlled mirrors (galvo scanners, see e.g. Zhang et al. (2009)), movable laser diode assemblies or bundles of optically multiplexed fibers (Davis et al. (2008)). While fibers require a more or less direct coupling with the surface of the object/animal, galvo scanners and movable laser diodes provide free-space scanning. Fiber-based systems usually do not move the animal but many free-space systems employ rotational and/or linear stages to move the animal so as to image it from different sides. A recently developed free-space system (Li et al. (2009)) includes a conical mirror which partially encloses the sample and thus collects significantly more light than a camera alone or systems with flat mirrors (see e.g. Chaudhari et al. (2005) in a non-fluorescent application). The conical mirror makes a rotational stage unnecessary because light can be collected from nearly all sides of the sample at once. The excitation beam is coupled to the sample via a galvo scanner and auxiliary optics. In addition, some systems include a laser-based surface scanner in order to provide the outer boundary shape of the animal under investigation (e.g. Li et al. (2009); Zavattini et al. (2006)).

3.4 Multispectral imaging

Multi- and hyperspectral imaging can improve the depth resolution of fDOT systems due to the strong wavelength dependence of absorption and scattering properties of tissue (Zavattini et al. (2006)). *Multispectral* means the collection of several (e.g. up to 10) different wavelengths while *hyperspectral* means the acquisition at many (e.g. 100) different wavelengths (Chaudhari et al. (2005)). Also excitation spectroscopy, i.e. the use of many excitation wavelengths, has been proposed and is even considered as preferable because the dependence of the absorption coefficient on the wavelength is stronger at shorter wavelengths, i.e. on the excitation side (Chaudhari et al. (2009)). While many fDOT systems developed so far operate at more than one excitation wavelength, spectroscopic detection is still not very widespread in tomographic systems. Recent examples were published by Zavattini et al. (2006), Li et al. (2009) and Zacharakis et al. (2011). Culver et al. (2003) developed a hybrid CW/frequency domain fDOT system for breast cancer imaging. This system needs a matching fluid and coupling of 45 detector fibers to the volume under investigation. Excitation is achieved with four selectable laser diodes with the wavelengths 650, 690, 786 and 830 nm, each of which can be modulated sinusoidally at 70 MHz. Nine fibers carry light to a PMT based demodulation stage while simultaneously a transmission image is captured with a CCD camera in CW mode. Li et al. (2009) published a CW system with two excitation lasers at 650 and 785 nm. Detection is possible at 9 spectral bands, which are spaced between 680 nm to 840 nm and have a width of 20 nm, thus allowing for excitation spectroscopy. Zavattini et al. (2006)

described a CW system with one moving excitation laser at 640 nm and a CCD camera based spectrograph. The spectrograph consists of a grating and an entrance slit which allows for a spectral resolution of 3 nm. The camera provides x-λ images, i.e. spatial information along one dimension (x) and spectral information between 400 nm to 1000 nm. A translational stage allows scanning along the second spatial dimension (y). Another recently published CW system comprises a CCD camera and a Czerny-Turner spectrograph as detection unit while exciting the animal at relatively short wavelengths, i.e. the 488 and 514 nm lines of an Argon laser (Zacharakis et al. (2011)). Zhang & Badea (2011) presented an improvement of the system developed by Zhang et al. (2009), thus not only allowing for time-gated time domain acquisition but also for multi-wavelength-excitation by the introduction of a tunable Ti:sapphire laser. The tuning range from 690 to 1040 nm provides the unique possibility of time resolved excitation spectroscopy, though in Zhang & Badea (2011) still no use was made of the tuning option.

3.5 Hybrid systems: Combining high resolution modalities with fDOT

fDOT images exhibit low resolution due to the massive scattering of photons in most biological tissues. The integration of good regularizing priors based on anatomical data, provided by e.g. CT or MRI, can lead to significant improvement of the image quality (Panagiotou et al. (2009); Zhang et al. (2009)) and is mandatory when following recent trends. This motivates the development of bimodal imaging systems which combine fDOT with high-resolution methods.

A laboratory system was described in da Silva et al. (2007); Silva et al. (2009), comprising an X-ray generator and a flat panel detector as well as a krypton laser (752 nm) and a CCD camera. The sample is rotated and translated in order to form the projections. In addition, the laser beam is steered via a movable mirror. A similar concept was used by Aguirre et al. (2008), i.e. a single laser diode with 675 nm a CCD camera, an X-ray source and flat panel detector as well as a galvo scanner. In contrast to (da Silva et al. (2007)) all components were mounted on a rotating gantry with 360° angular steering range.

More recently the optical units were integrated into commercial micro-CT devices: Schulz et al. (2010) reported a hybrid fDOT-CT system, which employs a free-space CW-fDOT equipment on the rotating gantry of a micro-CT device. Two fiber-coupled laser diodes (670 and 750 nm) are used as sources, the animal is scanned with an x-y-stage. The detector is a cooled CCD camera with a 50 mm macro-lens.

Yang et al. (2010) developed an fDOT-CT dual-modality system with a flat panel detector-based micro-CT for small animals. The CW-fDOT part relies on a 748 nm diode laser and a cooled CCD camera mounted orthogonally to the micro-CT and the projection images were acquired without rotation of the sample. Similarly, Lin et al. (2010) employed an X-ray CT system with 2 lasers at 785 and 803 nm as well as a cooled CCD camera on a rotating gantry.

All these XCT-fDOT systems operate only in CW-mode.

Only a few attempts have been made so far to build hybrid devices employing MRI as the high-resolution modality. Some pioneering work was already done in the field of DOT, e.g. by Ntziachristos et al. (2000) involving a fiber-optic interface for the investigation of the human breast inside of an MRI scanner. The optical instrumentation comprised a PMT-based

single-photon counting system. Masciotti et al. (2009) published an 9.4 T MRI small animal scanner with an animal coil (38 mm diameter) and a fiber-optic interface with 13 source fibers and 27 detection fibers. The system comprises two lasers at 757 and 828 nm, which can be modulated up to about 1 GHz. Homodyne demodulation is performed with a modulated ICCD. Davis et al. (2008) designed a spectroscopic CW fDOT unit, which is coupled to the animal bed inside a 3 T-MRI body scanner via fibers (8 detectors, 16 sources). The excitation laser operates at 690 nm. The animal bed is placed inside a specially designed rodent coil for MR-acquisition.

3.6 Advanced hardware concepts

As scanning time is an important issue in fDOT, reducing the required time for data acquisition is a challenging task. Wang et al. (2010) applied spatial encoding of the excitation light in order to reduce the time needed to create different excitation patterns. Several laser diodes are switched on in a particular pattern and moved in axial direction during the scanning process.

A completely different approach avoids source multiplexing completely, thus reducing hardware complexity significantly. In contrast to usual spatial encoding by various combinations of source/detector locations, only a single macro-illumination light source with a broad spectrum and a tunable excitation filter is used. The required spatial encoding is achieved by varying the excitation wavelength and exploiting the frequency-dependent sensitivity distribution inside of the target for the image reconstruction. A prototype (Klose & Pöschinger (2011)) consists of a commercial 2D-small animal imager with a white light source, a tunable filter and a cooled CCD camera. The excitation wavelength was varied in nine steps from 590 to 660 nm with a bandwidth of 10 nm per step. Fluorescence light was collected at 700 nm. The price paid for the simpler hardware setup is a more complex reconstruction algorithm which must contain a valid model of frequency-dependent light propagation in moderately absorbing tissues, which requires extensions of the popular diffusion approximation of the radiative transfer equation.

3.7 Comparison of technologies

It is intuitively clear that CW systems do not allow fluorescence lifetime imaging (FLIM) but besides it is also not possible to separately identify the absorption and scattering coefficients of the medium under investigation (Arridge & Lionheart (1998)). More sophisticated investigations thus require either the use of FDFT or TDFT. As the instrumentation is significantly less expensive and demanding for FDFT it would be desirable to contrast the two approaches in the context of information content and data quality. As mentioned, the information content is theoretically equal for both modalities when the same sources and detectors are applied and when the number of frequencies in FD corresponds to the number of time steps in TD. However, in time domain spectroscopy there are two apparent advantages from the instrumentation point of view. These are in particular: (i) Dark noise and PMT gain noise can be eliminated very effectively which is not the case for FDFT. (ii) Artifacts arising from e.g. reflections can be frequently sorted out prior to any subsequent data processing just by time-gating.

A rigorous comparison of the methods is difficult because it should include adequate noise models and cutting-edge reconstruction techniques, which exploit all the information

available in the data for both modalities. Moreover, parameters like the effective aperture of the detectors, power of the light sources and effective measurement time must be taken into account for a fair comparison. One attempt was made for diffuse optical tomography (DOT) by Nissilä et al. (2006) where the authors compared the time domain system of the University College London (UCL) (Schmidt et al. (2000)) and a frequency domain system developed at Helsinki University of Technology (HUT) (Nissilä et al. (2005)). Both systems are fiber-coupled but differ in the number of source and detector positions. Both systems operate in the NIR range at very similar wavelengths, i.e. 780 and 815 nm (UCL) and 760 and 830 nm (HUT), respectively. As the HUT system operates only at one single modulation frequency of 100 MHz a comparison can only be made in the context of time harmonic image reconstruction, i.e. in terms of magnitude and phase. Considering this limitation the noise data of both systems are similar, yielding an amplitude noise of 1.7 % and 0.5 % and a phase noise of 0.2 and 0.5°, respectively at a detected light power of 1 pW. However, the laser power was different (8 mW for HUT and 40 mW for UCL) and the acquisition speed was somewhat shorter in the HUT system. The authors of the article also list some data of other frequency domain systems and show that the HUT and UCL systems, at that time, had comparatively good noise performance and could thus serve as reference systems. The analysis also comprises image reconstruction results from data generated with both systems, but only based on a frequency domain approach. Therefore, this comparison cannot be generalized because it neither takes into account the full information content of time domain data nor the specific advantages of optimized time domain reconstruction algorithms. A more rigorous and comprehensive comparison including realistic noise models and adequate solvers for all modalities is still lacking.

4. Mathematical description of light transport

Before we can discuss reconstruction methods to find the fluorophore distribution inside an object, it is necessary to describe mathematical methods to model how light spreads inside an object. Nowadays, three models are commonly used which are—with decreasing accuracy—the Monte Carlo method, the radiative transport equation and its diffusion approximation.

4.1 Random-walk Monte Carlo method

Random-walk Monte Carlo (MC) methods for solving the forward model have a rather long tradition in optics and have been implemented in different flavors. In the most simple form, the path of a single photon throughout the tissue is simulated in every run. As most of the physical processes like the change of the polarization state or the absorption of photons by electron excitation are stochastic in their nature, MC methods are well suited to model these effects. Furthermore, it is comparatively easy to incorporate tissue inhomogeneities, reflection and refraction at internal boundaries due to variations in the index of refraction, anisotropic scattering phase functions and so on.

The drawback of MC methods is their slow convergence which is proportional to the square root of the number of runs. In order to achieve reliable results for three dimensional objects, it is often necessary to simulate the propagation of millions of photons. The convergence is also poor when a certain physical process has a very low probability, say it occurs only once in one thousand trials.

A series of strategies for speeding up the simulations has been developed, for example, simulating photon packets rather than individual particles (Wang et al. (1995)) and running photons in parallel using modern graphics hardware (Fang & Boas (2009)). Still, the comparatively high computational effort limits the applicability of Monte Carlo methods for reconstructing fluorophore properties.

4.2 Transport equation

A deterministic solution for light propagation can be found in Boltzmann's transport equation which is also frequently called the *radiative transport equation* (RTE). Rather than modeling each particle independently, which can be done with Monte Carlo methods, the RTE deals with an ensemble of photons in an infinitesimal volume. To be more precise, the RTE is a balance equation for the number of photons per unit volume (i.e. the photon density) $\Phi(\vec{x}, \hat{s}, t)$ at a spatial location $\vec{x}$ traveling into an infinitesimal solid angle around a direction $\hat{s}$ at a time instance t. The transport equation reads

$$\begin{aligned} \frac{1}{\nu}\frac{\partial \Phi(\vec{x},\hat{s},t)}{\partial t} + \hat{s}\cdot\nabla\Phi(\vec{x},\hat{s},t) + \left(\mu_a(\vec{x}) + \mu_s(\vec{x})\right)\Phi(\vec{x},\hat{s},t) \\ = q_{int}(\vec{x},\hat{s},t) + \mu_s(\vec{x})\int_{S^2}\Theta(\hat{s}',\hat{s})\Phi(\vec{x},\hat{s}',t)\,d\hat{s}' \qquad \text{in } \Omega, \end{aligned} \tag{1}$$

together with the boundary condition

$$\Phi(\vec{x},\hat{s},t) = q_{bc}(\vec{x},\hat{s},t) \qquad \forall \hat{s} : \hat{s}\cdot\hat{n} < 0 \qquad \text{on } \Gamma, \tag{2}$$

where ν is the speed of light in the tissue, μ_a and μ_s are the absorption and scattering coefficients, respectively, and $\Theta(\hat{s}', \hat{s})$ is the scattering phase function which states the probability that a photon traveling in direction $\hat{s}'$ will be deflected into direction $\hat{s}$. In this equation, S^2 is the surface of the unit sphere and thus the integral is taken over all possible directions. The term q_{int} models sources inside the domain.

The left-hand side of equation (1) models the decrease in photon density due to movement and absorption, while the right-hand side incorporates the photon gain caused by scattering and an internal source.

The boundary condition imposes restrictions on the solution only for inward-pointing directions, i.e. for all $\hat{s}$ with $\hat{s}\cdot\hat{n} < 0$ where $\hat{n}$ is the outward-pointing unit normal of the domain. It states that no light can enter the domain from the outside except at locations where a boundary source is present, i.e. where $q_{bc}(\vec{x},\hat{s},t) \neq 0$.

A limitation of the transport equation is that it cannot handle wave effects. As a consequence, the wavelength of the light must be much smaller than the dimensions of the structures in the domain (Gibson et al. (2005)). Furthermore, varying indices of refraction are not included in equation (1) but can be incorporated.

Despite these insufficiencies, the transport equation would be well suited for biomedical optics. It is able to handle many different types of tissue whether they are highly scattering like muscle, as absorbing as the liver or as transparent as liquor, for example. Furthermore, the boundary equation is physically meaningful.

The reason why the RTE is frequently avoided is the high computational effort required for calculating an accurate solution. The photon density $\Phi(\vec{x},\hat{s},t)$ has to be discretised in the

spatial and angular domain which requires five variables for a 3D problem (three coordinates and two angles). If too little angular directions are chosen for the discretisation, the resultant photon field favors propagation along these directions resulting in star-like patterns, where one would expect a radial symmetric distribution instead. To illustrate the influence of the angular discretisation on the computational effort, imagine a rather coarse discretisation of only 32 divisions for both the azimuth and the inclination. This results in 1024 angular directions, which have to be multiplied by the number of mesh points used for the spatial discretisation.

4.3 Diffusion approximation

Due to the shortcomings of the previously mentioned models, the most common description for photon migration is the diffusion approximation. This is a reduced form of the RTE which first expands the direction-dependent quantities Φ, Θ, q_{int} and q_{bc} into spherical harmonics. Then, all spherical harmonics except the first one are neglected, i.e. only the isotropic propagation of photons is considered. Some additional constraints are imposed on the photon flux and the scattering phase function Θ. A thorough derivation is found in the review article by Arridge (1999). The model is valid in the regime where photon propagation is diffuse, which is the case in tissues which are much more scattering than absorbing, at a sufficient distance from the source. Problems arise if the tissue is either strongly absorbing such as in the liver or nearly transparent as in liquor. Furthermore, the model is inaccurate near the light source, where the photon propagation is not yet diffuse due to the small number of scattering events, and at places where the optical properties jump which might be the case at the boundary of organs, for example (Gibson et al. (2005)).

In its frequency domain form, the diffusion approximation is a partial differential equation (PDE) which reads

$$-\nabla \cdot (\kappa(\vec{x})\nabla\varphi(\vec{x})) + \left(\mu_a(\vec{x}) + \frac{i\omega}{\nu}\right)\varphi(\vec{x}) = q_{int}(\vec{x}), \qquad \text{in } \Omega, \tag{3}$$

$$\varrho\varphi(\vec{x}) + \kappa(\vec{x})\hat{n}\cdot\nabla\varphi(\vec{x}) = \begin{cases} \varrho\, q_{bc}(\vec{x}), & \text{on } \Gamma_{bc}, \\ 0, & \text{on } \Gamma \setminus \Gamma_{bc}, \end{cases} \tag{4}$$

where φ is the fluence, $\kappa = (3(\mu_s' + \mu_a))^{-1}$ the diffusion coefficient of the tissue, μ_s' the reduced scattering coefficient and μ_a the absorption coefficient. ω is the modulation frequency of the excitation light source with the special case of $\omega = 0\,\mathrm{s}^{-1}$ for CW excitation with a constant intensity. The injected light can be modeled by an internal source q_{int} ,which is frequently used for collimated beams, or a boundary source q_{bc}, which is suitable for spatially extended sources on a part Γ_{bc} of the boundary Γ. ϱ is a reflection coefficient to incorporate the reflections at the boundary Γ of the domain Ω due to the differences in the indices of reflection.

4.4 Diffusion approximation for fDOT

For fDOT, the diffusion approximation has to be extended as now two different photon distributions with different wavelengths have to be simulated: (i) excitation light due to the illumination of the sample and (ii) emission light which has been generated by a fluorophore inside the sample by conversion from the excitation wavelength. As the optical parameters of tissue vary with the chosen wavelength, we distinguish them by sub-scripts x and m for excitation and emission, respectively. Furthermore, these coefficients have to depend on the

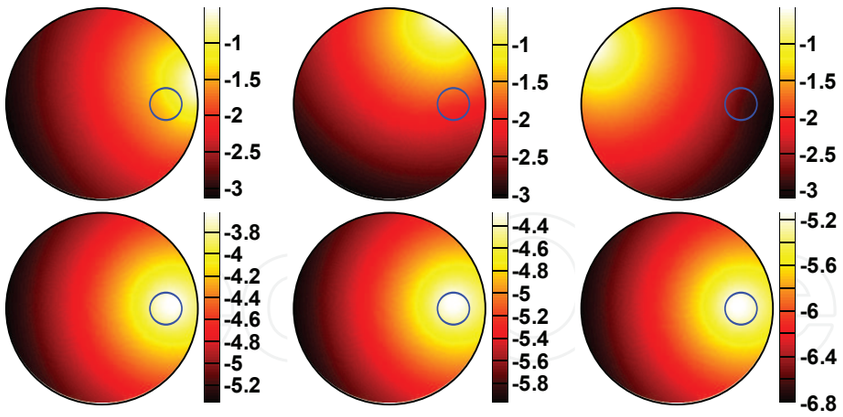

Fig. 3. Simulation of the fluences $\varphi_x(\vec{x})$ (top row) and $\varphi_m(\vec{x})$ (bottom row) due to three different boundary sources positioned at angles of 11.25° (left), 56.25° (middle) and 146.25° (right). The color encodes the logarithm of the amplitude of the photon densities.

fluorophore concentration $c(\vec{x})$ which one seeks to reconstruct from measurements in a known manner. If the concentration is fairly small, it can be seen as an additional absorber and the effective absorption coefficients can be written in the form

$$\mu_x(\vec{x}) := \mu_{a,0,x}(\vec{x}) + \epsilon_x\, c(\vec{x}) + \frac{i\omega}{\nu} \qquad \text{and} \tag{5}$$

$$\mu_m(\vec{x}) := \mu_{a,0,m}(\vec{x}) + \epsilon_m\, c(\vec{x}) + \frac{i\omega}{\nu}, \tag{6}$$

where $\mu_{a,0,i}$, $i \in \{x, m\}$, is the background absorption of the tissue in the absence of fluorescent agent and ϵ_x, ϵ_m are the molar extinction coefficients which relate the fluorophore's concentration to its absorption coefficients. With these definitions the diffusion approximation for fDOT can be written as a two-state model (Sevick-Muraca et al. (2003)):

$$-\nabla\cdot(\kappa_x(\vec{x})\nabla\varphi_x(\vec{x})) + \mu_x(\vec{x})\varphi_x(\vec{x}) = q_{int}(\vec{x}), \qquad \text{in } \Omega, \tag{7}$$

$$-\nabla\cdot(\kappa_m(\vec{x})\nabla\varphi_m(\vec{x})) + \mu_m(\vec{x})\varphi_m(\vec{x}) = \frac{\eta}{1+i\omega\tau}\epsilon_x\, c(\vec{x})\varphi_x(\vec{x}), \qquad \text{in } \Omega, \tag{8}$$

with the boundary conditions

$$\varrho_x\varphi_x(\vec{x}) + \kappa_x(\vec{x})\hat{n}\cdot\nabla\varphi_x(\vec{x}) = \begin{cases} \varrho_x q_{bc}(\vec{x}), & \text{on } \Gamma_{bc}, \\ 0, & \text{on } \Gamma\setminus\Gamma_{bc}, \end{cases} \tag{9}$$

$$\varrho_m\varphi_m(\vec{x}) + \kappa_m(\vec{x})\hat{n}\cdot\nabla\varphi_m(\vec{x}) = 0, \qquad \text{on } \Gamma. \tag{10}$$

The conversion efficiency of the fluorophore is denoted by the constant η and its fluorescent lifetime by τ. A typical simulation result is depicted in Figure 3.

The measurement data is gathered by illuminating the sample with differently positioned light sources and recording the photons leaving the boundary. The simplest type of measurement is to record the photons leaving the boundary at a certain location, i.e. to integrate the photon flux over a detector area χ:

$$-\int_\Gamma \kappa_m(\vec{x})\hat{n}\cdot\nabla\varphi_m(\vec{x})\chi(\vec{x})\,d\vec{x} \overset{(10)}{=} \varrho_m\int_\Gamma \varphi_m(\vec{x})\chi(\vec{x})\,d\vec{x}. \tag{11}$$

The detector function χ can also incorporate linear transfer characteristics of the system such as a weighting due to an oblique viewing angle when using a camera. Other types of measurements based on the logarithm of the intensity, for example, have been reported in e.g. Arridge (1995); Arridge & Schweiger (1993); Sevick & Chance (1991).

As for a tomographic measurement N_s light sources and N_d detectors are used, the data can be written in a matrix $\mathcal{M}$ of size $N_d \times N_s$. The emission field φ_m depends on the fluorophore concentration c, which makes the measurement matrix dependent on c and we write $\mathcal{M}(c)$ to emphasize this fact.

5. Image reconstruction

The aim of fluorescence tomography is to reconstruct the fluorophore concentration and/or the fluorophore's lifetime inside a 3D object from intensity measurements performed on the object's boundary. In the previous section, methods have been described to simulate the photon propagation inside an object, where the tissue and fluorophore properties are known exactly. This is called the *direct* or *forward problem*. The estimation of the fluorophore distribution from measurement data is known as the *inverse problem* of fluorescence tomography. An overview about the whole reconstruction process is displayed in Figure 4. In the following, more details will be provided for solving this problem. For the sake of simplicity, the focus is put on FDFT-systems, whose mathematics is easier to grasp. Furthermore, one can Fourier-transform time domain data and apply FDFT-algorithms. Last but not least, CW-reconstructions are a special case of FDFT-reconstructions with a modulation frequency of $\omega = 0\,\mathrm{s}^{-1}$.

Mathematically the problem can be formulated as follows: Let $\mathcal{M}^\delta$ denote a light measurement taken at the object's surface, which is usually perturbed by noise bounded by δ coming from different origins, e.g. detector noise, discretisation errors and modeling errors. Then, one seeks to find a fluorophore concentration c such that the data mismatch $\left\| \mathcal{M}(c) - \mathcal{M}^\delta \right\|^2$ is minimized.

5.1 Ill-posedness of the inverse problem

Fiber-coupled fDOT systems usually result in a limited amount of data. Configurations with approximately 16 sources and 16 detectors are common which gives a set of 256 measurements. The inverse problem is under-determined in this case: there is much less measurement data than the number of voxels (typically in the order of ten-thousands) in which we would like to compute the fluorophore concentration.

The situation is different for the free-space arrangement. The camera can take images of the whole surface (which depends quadratically on the object's dimension d). If also the excitation beam can be positioned everywhere at the surface, one would get measurement combinations in the order of $d^2 \times d^2 = d^4$ but needs to reconstruct only d^3 voxels. In this case more measurement data is available than there are unknown parameters and the problem is said to be over-determined.

However, we cannot expect to reconstruct high-resolution images similar to CT from fluorescence tomography data. In CT the X-ray beams pass the object under investigation in nearly straight lines as illustrated in Figure 5(a). If the X-ray hits an absorbing object (the small

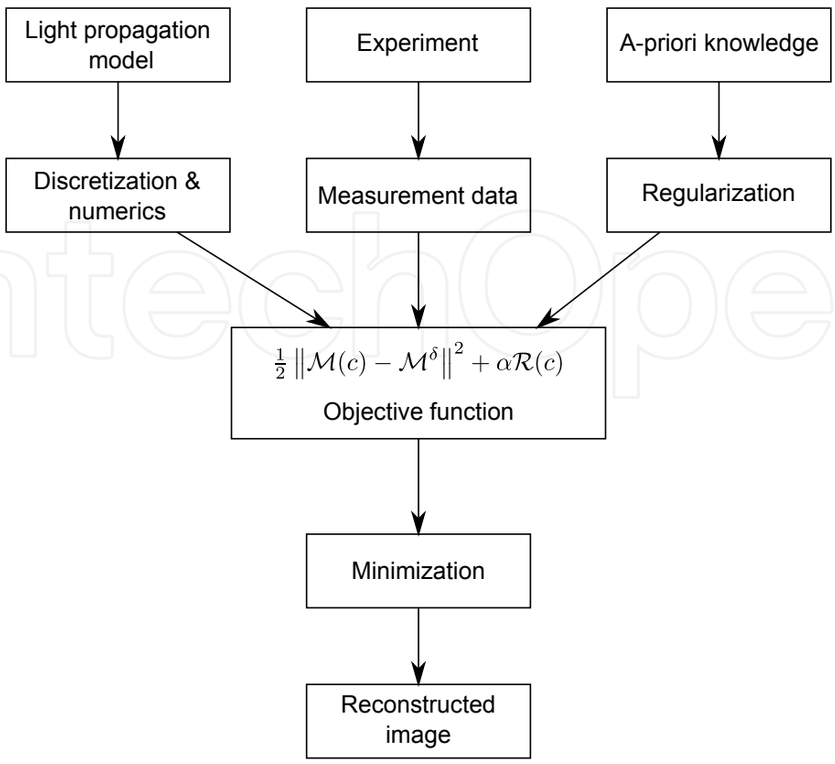

Fig. 4. Typical image reconstruction process: With the help of appropriately discretized mathematical models the simulated measurement data $\mathcal{M}(c)$ is computed. The simulated measurements have to be close to the true data $\mathcal{M}^{\delta}$ gathered from experiments. A regularization term $\mathcal{R}(c)$ has to be created from a-priori knowledge, which is needed to stabilize the algorithm. Finally, the image is reconstructed by minimizing the sum of the data mismatch and the penalty term.

ball), it is partly absorbed which casts a "shadow" in the recorded intensity projection I. In fDOT the photons are massively scattered and spread throughout the whole object. Figure 5(b) shows the distribution of the light emitted by a fluorescent ball when a small part of the surface at the top is illuminated with light. A camera looking at the object's bottom records a much more diffuse light intensity pattern compared to the CT detector. The interface between the fluorescent object and the background cannot be determined from these measurements directly.

An important quantity for the solution of the inverse problem is the so-called *sensitivity*. It measures the influence of a change in an image voxel onto a detector datum. This concept is illustrated for CT and fDOT in Figure 6: The sensitive area of an X-ray beam which is generated by a source S and detected by D consists of all voxels along the line which the X-ray passes. Analogously, an fDOT measurement is sensitive in that region which photons generated by the source S and recorded by the detector D traverse. Due to the massive scattering, the resulting fDOT sensitivity profile is much broader than the one from CT. In other words, a single fDOT measurement incorporates information from nearly the whole sample volume, while a CT datum only measures along a line.

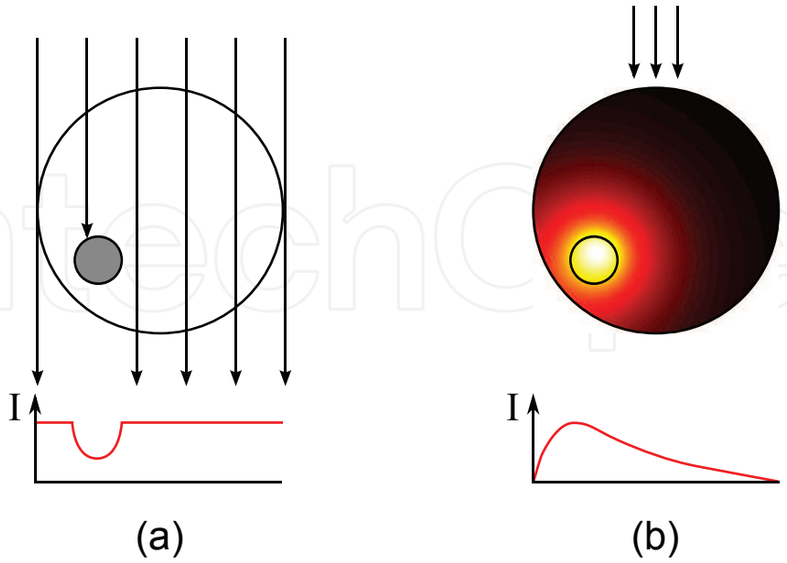

Fig. 5. Comparison between CT (a) and fDOT (b). In a CT system the X-ray beams pass the sample in nearly straight lines. The intensity I decreases if an absorbing object is encountered resulting in a "shadow" projection. In fDOT the emission light (shown in color) spreads throughout the sample although the surface is excited at a very small patch only. The intensity profile which a camera would record from the bottom is much more diffuse than the CT projection.

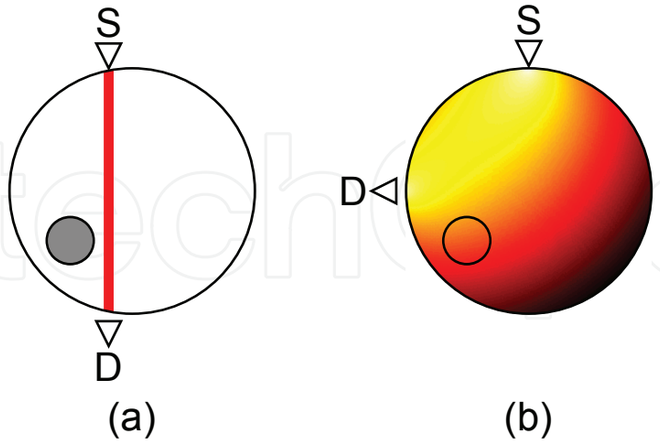

Fig. 6. Sensitivity profile for a single CT- and fDOT-measurement. (a) The voxels to which a CT measurement is sensitive lie along the line which the X-ray beam passes. (b) The photons in fDOT have a much larger coverage than an X-ray beam which leads to a broadening of the sensitivity profile.

An elegant way to compute the sensitivity mathematically is through the use of *adjoint* fields. These fields are generated by formally treating the detectors as sources which generate an adjoint photon distribution. The adjoint field is a spatially resolved measure for the detection efficiency of a sensor. The sensitivity at a certain position in the sample is then the product of the forward field (the photon distribution due to the light source) times the adjoint field (the distribution of the photon collection efficiency). It is highest at locations which are reached by many photons from the source and from which many photons are collected by the detector *at the same time*.

The adjoint system to the forward system (7)–(10) is another system of PDEs which reads

$$-\nabla\cdot(\kappa_m(\vec{x})\nabla\psi_m(\vec{x}))+\overline{\mu}_m(\vec{x})\psi_m(\vec{x})=0 \qquad \text{in } \Omega \tag{12}$$

$$-\nabla\cdot(\kappa_x(\vec{x})\nabla\psi_x(\vec{x}))+\overline{\mu}_x(\vec{x})\psi_x=\frac{\eta}{1-i\omega\tau}\epsilon_x\, c(\vec{x})\psi_m(\vec{x}) \qquad \text{in } \Omega \tag{13}$$

$$\varrho_m\psi_m(\vec{x})+\kappa_m(\vec{x})\hat{n}\cdot\nabla\psi_m(\vec{x})=\varrho_m\chi(\vec{x}) \qquad \text{on } \Gamma \tag{14}$$

$$\varrho_x\psi_x(\vec{x})+\kappa_x(\vec{x})\hat{n}\cdot\nabla\psi_x(\vec{x})=0 \qquad \text{on } \Gamma. \tag{15}$$

The sensitivity of the ij-th measurement around c into direction h is given by

$$\begin{aligned}\mathcal{M}'_{ij}(c)h &:= \lim_{h\to 0}\frac{\mathcal{M}_{ij}(c+h)-\mathcal{M}_{ij}(c)}{\|h\|}\\ &= -\int_\Omega \kappa'_x h\,\nabla\varphi_x(q_j)\cdot\nabla\overline{\psi}_x(\chi_i)\,d\vec{x}-\int_\Omega \mu'_x h\,\varphi_x(q_j)\overline{\psi}_x(\chi_i)\,d\vec{x}\\ &\quad -\int_\Omega \kappa'_m h\,\nabla\varphi_m(q_j)\cdot\nabla\overline{\psi}_m(\chi_i)\,d\vec{x}-\int_\Omega \mu'_m h\,\varphi_m(q_j)\overline{\psi}_m(\chi_i)\,d\vec{x}\\ &\quad +\frac{\eta}{1+i\omega\tau}\epsilon_x\int_\Omega h\,\varphi_x(q_j)\overline{\psi}_m(\chi_i)\,d\vec{x}.\end{aligned} \tag{16}$$

In this equation, we used the notation $\varphi(q_j)$ and $\varphi(\chi_i)$ to emphasize the dependencies of the forward field on the excitation source q_j and the adjoint field on the detector χ_i, respectively.

When solving the inverse problem, one seeks to reconstruct the parameters in the sensitive area from the measurement data. Looking at Figure 6, it is intuitively clear that this task is much easier for CT, where one can simply distribute a measurement datum back along the line which the X-ray beam passed, than for fDOT, where every recording has to be distributed in the whole sample. This lack of information is valid for both fiber-based and free-space arrangements. The reconstruction problem is said to be *ill-posed*.

5.2 The role of prior information

To deal with the ill-posedness of the inverse problem, additional knowledge has to be incorporated into the reconstruction algorithm which is known as *regularization*. This means that unphysical or undesired images are penalized while images featuring certain characteristics are favored. Using regularization terms of Tikhonov-type, one can state the image reconstruction as an optimization problem, where one seeks to minimize the functional

$$\mathcal{L}_\alpha(c) := \tfrac{1}{2}\left\|\mathcal{M}(c)-\mathcal{M}^\delta\right\|^2+\alpha\mathcal{R}(c). \tag{17}$$

In this equation, $\mathcal{R}(c)$ is a penalty for unwanted fluorophore distributions. With the parameter α it is possible to adjust between sticking to the data ($\alpha = 0$, which means no regularization at all) and reconstructing a concentration according to the prior information ($\alpha \to \infty$, which means that the simulated and the measured data can diverge arbitrarily). As the problem (17) is non-linear, one can choose e.g. Newton methods to solve it. If the Hessian (i.e. the second derivatives of the forward operator $\mathcal{M}(c)$) is neglected, one can write the iterations in the form

$$\mathrm{Re}\left\{\mathcal{M}'^{*}(c_k)\mathcal{M}'(c_k) + \alpha_k \widetilde{\mathcal{R}}''(c_k)\right\}\Delta c_k = \mathrm{Re}\left\{\mathcal{M}'^{*}(c_k)\left(\mathcal{M}^{\delta} - \mathcal{M}(c_k)\right) - \alpha_k \mathcal{R}'(c_k)\right\}, \quad (18)$$

where the parameter α can vary in every iteration. This is known as the iteratively regularized Gauß-Newton algorithm and is treated in detail elsewhere (Bakushinskiĭ (1992); Blaschke et al. (1997); Engl et al. (1996)). In this context, $\mathcal{M}'^{*}$ means the adjoint of the sensitivity operator $\mathcal{M}'$ and its exact meaning depends on the chosen discretisation. $\mathcal{R}'(c_k)$ and $\widetilde{\mathcal{R}}''(c_k)$ are the first and approximated second derivatives of the regularization term evaluated for the current concentration c_k. Besides the Gauß-Newton method, other algorithms are available such as the Levenberg-Marquardt method (Marquardt (1963)), the Newton-Landweber method (Kaltenbacher (1997)) and the truncated Newton-CG method (Hanke (1997)). Applications to the field of optical tomography are e.g. Egger & Schlottbom (2011); Jiang (1998); Joshi et al. (2004); Roy & Sevick-Muraca (1999); Schweiger et al. (2005). A good overview of reconstruction methods applied to fluorescence tomography is given by Sevick-Muraca et al. (2003).

Unfortunately, there is no one-size-fits-all-type regularization method. Instead, $\mathcal{R}(c)$ has to be chosen with respect to the application and the expected outcome. In the following, typical regularization methods are discussed.

5.2.1 Quadratic regularization terms

The probably most often used regularization term is the L^2-norm of the concentration, which is a penalty for large concentrations such as outliers. Thus, smaller values for the concentration in the whole domain are preferred. The dominance of this particular regularization term in many engineering applications is most likely not not due to its physical meaning but rather due to its simplicity and speed, both in implementation and evaluation. If we denote the identity operator with I, the regularization term and its derivatives can be written as

$$\mathcal{R}(c) = \tfrac{1}{2}\|c\|^2, \qquad \mathcal{R}'(c) = c, \qquad \mathcal{R}''(c) = I. \quad (19)$$

If one can provide an a-priori guess c_0 for the fluorophore distribution, it is advantageous to penalize the difference between the prior guess and the current concentration, i.e. to use a regularization term of the form

$$\mathcal{R}(c) = \tfrac{1}{2}\|c - c_0\|^2. \quad (20)$$

Another quadratic regularization term is based on the H^1-semi-norm instead of the L^2-norm. This semi-norm does not penalize higher concentration values but it penalizes variations in the reconstructed fluorophore distribution and thus enforces the resultant images to be

smooth. From a physical point of view, this is most often more meaningful than to suppress outliers. The regularization functional is defined as

$$\mathcal{R}(c) = \tfrac{1}{2}\|\nabla c\|^2, \qquad \mathcal{R}'(c)h = \langle \nabla c, \nabla h \rangle, \qquad \langle \mathcal{R}''(c)h_1, h_2 \rangle = \langle \nabla h_1, \nabla h_2 \rangle. \tag{21}$$

5.2.2 Total-variation regularization

Although the H^1-semi-norm is physically meaningful, it faces the problem that large gradients of the fluorophore concentration are still penalized which prevents steep transitions (jumps) from an object to the background. However, if one knows a-priori that the fluorophore is well localized (e.g. inside a localized tumor) and piecewise constant, the total-variation (TV) regularization might be an option. Although this method also measures the gradient of the reconstructed image, it uses an L^1-norm rather than the L^2-norm for penalization:

$$\mathrm{TV}(c) := \int_\Omega |\nabla c(\vec{x})|\, d\vec{x}. \tag{22}$$

Using the L^1-norm, the penalty grows linearly with the gradient (instead of quadratically), i.e. larger gradients are allowed to some extent.

Unfortunately, the TV functional is not differentiable at points where $\nabla c(\vec{x}) = 0$. A possible mitigation is to use a relaxation as suggested by Acar & Vogel (1994) which reads

$$\begin{aligned} \mathcal{R}(c) &= \int_\Omega \sqrt{\beta + |\nabla c(\vec{x})|^2}\, d\vec{x}, \qquad \mathcal{R}'(c)h = \int_\Omega \frac{\nabla c(\vec{x}) \cdot \nabla h(\vec{x})}{\sqrt{\beta + |\nabla c(\vec{x})|^2}}\, d\vec{x}, \\ \left\langle \widetilde{\mathcal{R}}''(c)h_1, h_2 \right\rangle &= \int_\Omega \frac{\nabla h_1(\vec{x}) \cdot \nabla h_2(\vec{x})}{\sqrt{\beta + |\nabla c(\vec{x})|^2}}\, d\vec{x} \end{aligned} \tag{23}$$

where a scalar $\beta > 0$ has been introduced to smooth the square-root around the origin. Note also that $\widetilde{\mathcal{R}}''$ is just an approximation of the true Hessian, because the derivative of the denominator has been neglected.

5.2.3 Level-set method

Another possibility of regularization is through the use of level-set methods, which have been used for diffuse optical tomography (Alvarez et al. (2009); Schweiger et al. (2008)). The principle is that if the background fluorescence and the fluorescence inside and object are constant, the reconstruction problem reduces to finding the interface which separates the inclusions from the background. This interface can be described using level-set methods: The level-set function $\phi(\vec{x}), \vec{x} \in \Omega$ is negative inside the inclusion and positive outside. Thus, the separating interface consists of all points where the level-set function is zero, i.e. it is the zero-level set $\{\vec{x} : \phi(\vec{x}) = 0\}$. Applying the Heaviside function

$$H(z) := \begin{cases} 1, & z \geq 0, \\ 0, & \text{else}, \end{cases} \tag{24}$$

one can express the concentration distribution as the sum

$$c(\vec{x}) = c_{in} + H(\phi(\vec{x}))(c_{out} - c_{in}), \tag{25}$$

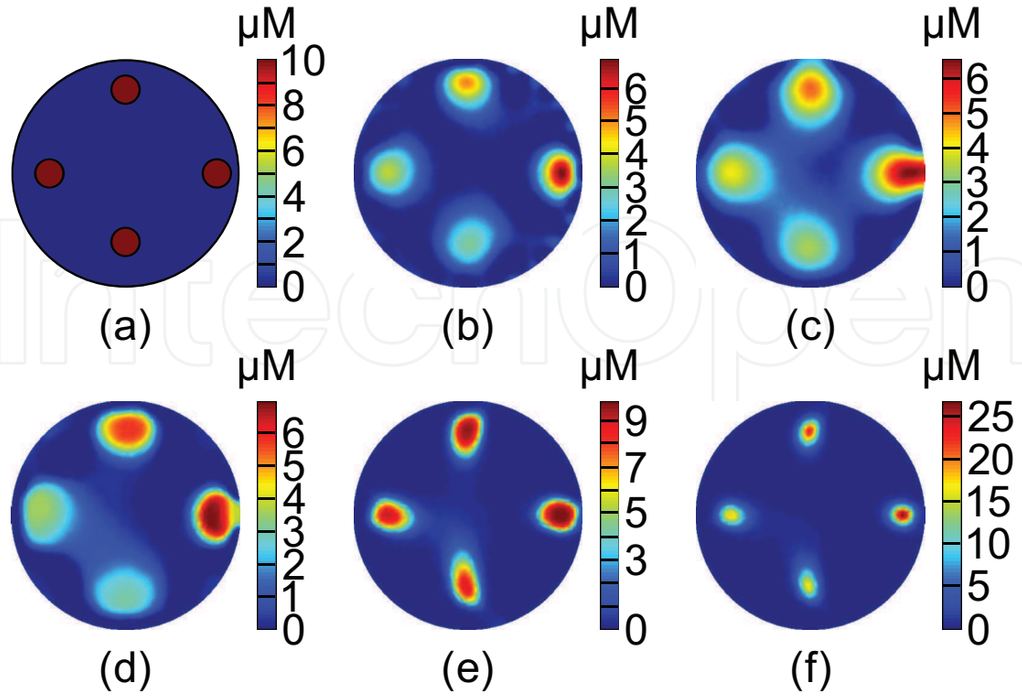

Fig. 7. Comparison of reconstructions of (a) four fluorescent objects with a concentration of 10 µM each. The reconstructions are based on (b) the L^2-norm, (c) the H^1-norm (d) the total-variation. Also the results from a method of level-set type with $c_{out} = 10\,\mu\text{M}$ are presented with two different levels for the concentration inside the object: (e) $c_{in} = 10\,\mu\text{M}$ and (f) $c_{in} = 50\,\mu\text{M}$.

where c_{out} and c_{in} are the two scalar fluorophore concentrations in the background and inside the inclusion.

Unfortunately, the numerical effort for the computation of the evolution of the level-set function is comparatively high. The reason is again the non-differentiability of the Heaviside function. A mitigation has been studied as a *method of level-set type* in Frühauf et al. (2005) and Egger & Leittão (2009). The idea is to parametrize the concentration c by a nonlinear, smooth, monotonically increasing function $H_\beta(\phi)$ and to reconstruct the level-set function ϕ which is done by minimizing the objective function

$$\mathcal{L}_\alpha^\phi = \tfrac{1}{2}\|F(H_\beta(\phi))\|^2 + \alpha\mathcal{R}(\phi). \tag{26}$$

One possible parametrization is by using the error function such that the approximated Heaviside reads

$$H_\beta(z) := \frac{c_{in} + c_{out}}{2} + \frac{c_{in} - c_{out}}{2}\,\text{erf}\left(\frac{z}{\beta}\right). \tag{27}$$

This parametrization restricts the concentration by the lower and upper bounds c_{out} and c_{in}, respectively, but still allows values in between. Furthermore, it has a smooth derivative which is useful for the Gauß-Newton algorithm.

Example reconstructions using the different kinds of regularization methods, which have been presented in this chapter, are shown in Figure 7.

5.2.4 Multi-modality regularization

When combining fDOT with a high-resolution modality such as CT or MRI, it is advantageous to use information from the highly resolved anatomical images to improve the quality of fDOT-reconstructions. In the following, some attempts for incorporating this information are listed.

In the work by Davis et al. (2007), the anatomical images were segmented and the regularization term $\mathcal{R}(c)$ was constructed such that it allows larger variations between voxels from different segments but keeps variations between voxels from the same segment small.

Although only applied to DOT, Douiri et al. (2007) used a-priori edge information (which could be obtained from CT, for example) together with an anisotropic diffusion model which preserves sharp edges in the reconstructed optical properties. This method could also be extended to fDOT to constrain the leakage of fluorescent agent in the reconstruction across anatomical boundaries.

Another approach, which uses segmented images from a high-resolution modality like MRI or CT, was presented by Hyde et al. (2010). Their algorithm first uses only one fluorescence concentration for each segment (thus reducing the dimension of the reconstruction problem) and creates a spatially-varying regularization matrix from the low-dimensional reconstruction in a second step.

5.3 Regularisation parameter and stopping criterion

The choice of the regularization parameter α in equation (17) has attracted quite some interest. The basic problem is that this parameter balances the *goodness of fit*, i.e. how well the mathematical model approximates the measured data, and the stability of the inversion. For the iteratively regularized Gauß-Newton algorithm, typically exponentially decaying sequences are suggested (Blaschke et al. (1997); Engl et al. (1996)).

Another problem is the stopping criterion for the iterative reconstruction. Most often these criteria are implemented using heuristics. For example, one can set a lower limit for the regularization parameter or stop if stagnation occurs and the residual no longer changes as done by Dehghani et al. (2008). Note that for the latter approach a good choice for the step length is mandatory. Otherwise, the residual will decrease very slowly which triggers the stopping criterion even when no (local) minimum of the objective functional has been reached.

An objective stopping criterion is given by Morozov's discrepancy principle (Morozov (1966)). It states that the residual shall not be smaller than the error in the measurement. Thus, if the true measurement without any noise is denoted as $\mathcal{M}$, α should be chosen such that

$$\|\mathcal{M}(c_\alpha) - \mathcal{M}^\delta\| \approx \|\mathcal{M} - \mathcal{M}^\delta\|, \tag{28}$$

where c_α denotes the reconstructed fluorophore distribution with regularization parameter α. In other words, the difference between the simulated measurement and the noisy data should be approximately the same as the difference between the (inaccessible) measurement values and the noisy data. Unfortunately, the expression on the right-hand side cannot be evaluated in practice as the true measurements $\mathcal{M}$ are not known. Thus, one has to deduce this quantity by other means based on the distribution of the noise, for example.

6. Recent developments for pre-clinical and clinical applications

2D fluorescence imaging in pre-clinical sciences is a well-established technology. In this section, we would like to give an overview about applications of truly three-dimensional fluorescence imaging. There are many publications showing the potential of fDOT in phantoms or ex-vivo while the number of in-vivo studies is still very limited. However, as in-vivo molecular imaging is probably the most attractive future field of application, this subchapter summarizes some important in-vivo results.

From the technological point of view, we can observe two major groups of applications, the first of which serves for the non-quantitative visualization of molecular or cellular processes, mostly evaluating quantum yield data. The second group tackles the more challenging field of quantitative imaging, frequently exploiting both quantum yield and fluorescence lifetime imaging (FLIM). The reconstruction of the fluorescence lifetime is of particular interest because it yields more reliable information about the chemical interaction of the probe with its environment than the fluorophore's quantum efficiency (Lakowicz (2006)).

In the first group we find e.g. the use of a cathepsin-activatable fluorescence probe by Niedre et al. (2008) to monitor a mouse lung tumor and by Haller et al. (2008) for the visualization of pulmonary inflammation. Another example is the visualization of macrophage infiltration of infarcted mycardium in a mouse model by Sosnovik et al. (2007), who compared MRI, planar fluorescence imaging and fluorescence tomography. Kozloff et al. (2007) investigated the feasibility of localizing bone mineralization/demineralization processes with a specific fluorescent probe in mice. So-called far-red fluorescent pamidronate (FRFP) was proven to specifically bind to bone mineral sites and fDOT images made with a commercial system enabled the visualization of deep mineralizing structures including the growth plates in the femoral heads. Biswal et al. (2011) developed a 2-nitroimidazole-ICG probe for monitoring tumor hypoxia and present images of tumors of sizes of a few millimeter, however, without assessing the accuracy of the tumor location and size in the reconstructions. Tan et al. (n.d.) used fluorescence tomography to monitor stem cells in Drosophila Pupae by the expression of a DsRed reporter.

In the second group (FLIM) we find a paper by Nothdurft et al. (2009) who were the first to show in-vivo life-time tomography on mice, where they imaged agarose gel implants as well as a cypate-labeled tumor. Gaind et al. (2010) showed the feasibility of reconstructing fluorescence resonance energy transfer (FRET) parameters, including the nanometer donor-acceptor distance, also from deep tissue regions in a mouse. 3D-studies of inter- and intra-molecular FRET could be of high importance for the investigation of diseases like Alzheimer's and some cancers related to protein misfolding. McGinty et al. (2011) presented FLIM in combination with Förster resonance energy transfer (FRET). In their experiment, a mouse genetically expressed a eGFP-mCherry-FRET probe.

So far there are only very few attempts to apply fluorescence tomography in human applications. The main reasons are certainly (i) the limited penetration depth of light in tissue which precludes the application of fDOT in extended parts of the body and (ii) the lack of approval for human use of most fluorescent labels known in molecular imaging. Corlu et al. (2007) presented a proof-of-concept study utilizing fluorescence tomography for detecting breast cancer in women using ICG as fluorescent agent. An interesting recent application for breast cancer imaging was reported by Mastanduno et al. (2011). The authors combined breast DCE-MRI, diffuse optical tomography and fDOT for imaging nine healthy volunteers

and one patient with breast cancer. fDOT was used for the reconstruction of autofluorescence from protoporphyrine IX, thus no extrinsic labeling agents were applied. The results, though lacking statistical power, suggest that combined application of all three modalities may provide improved information on malignancy when compared with DCE-MRI alone.

7. Trends and outlook

In this chapter, we addressed hardware-issues and reconstruction principles for fluorescence tomography and presented promising applications especially for pre-clinical sciences.

In the near future, we expect that more compact fluorescence tomography hardware will be developed e.g. through the replacement of photomultiplier tubes by silicon APDs. Another development will focus on hybrid devices such as fDOT/CT and fDOT/MRI combinations to use all the information from different modalities.

The reconstruction algorithms will on the one hand follow the hardware development, i.e. reliable strategies for the incorporation of a-priori information from CT and MRI into fDOT-images will be needed. On the other hand, the recent developments in commodity parallel computing architectures, such as modern graphics hardware with NVIDIA's CUDA toolkit or the OpenCL framework, will certainly aid the implementation of advanced algorithms including e.g. non-linear image regularization.

fDOT so far appears difficult to be used for human imaging. However, if autofluorescence could be used for producing diagnostically relevant contrasts, some niche-applications may arise. A recent example is the work by Mastanduno et al. (2011) which may open a new application window in breast imaging. Another important decisive issue is whether new fluorescent contrast agents will be approved for the use in humans.

In the field of pre-clinical imaging fDOT has been demonstrated to be feasible and the availability of commercial devices will certainly increase its use and importance. Current challenges are quantification and 3D lifetime imaging. As FLIM paves the way for 3D sensing of chemical analytes, this could be a new attractive field of research. Some pioneering work was already done by Shives et al. (2002) who showed the feasibility of FLIM-based oxygen sensing in-vitro and there is certainly potential for future developments towards in-vivo applications.

8. References

Acar, R. & Vogel, C. R. (1994). Analysis of bounded variation penalty methods for ill-posed problems, *Inv. Probl.* 10: 1217–1229.

Aguirre, J., Sisniega, A., Ripoll, J., Desco, M. & Vaquero, J. J. (2008). Design and development of a co-planar fluorescence and x–ray tomograph, *IEEE Nuclear Science Symposium Conference Record*, IEEE, pp. 5412–5413.

Alvarez, D., Medina, P. & Moscoso, M. (2009). Fluorescence lifetime imaging from time resolved measurements using a shape-based approach, *Opt. Express* 17: 8843–8855.

Arridge, S. R. (1995). Photon-measurement density functions. part I: Analytical forms, *Appl. Opt.* 34(31): 7395–7409.

Arridge, S. R. (1999). Optical tomography in medical imaging, *Inv. Probl.* 15: R41–R93.

Arridge, S. R. & Lionheart, W. R. B. (1998). Non–uniqueness in diffusion–based optical tomography, *Opt. Lett.* 23: 882–884.

Arridge, S. R. & Schweiger, M. (1993). The use of multiple data types in time-resolved optical absorption and scattering tomography (TOAST), *in* D. C. Wilson & J. N. Wilson (eds), *Mathematical Methods in Medical Imaging II*, Proc. Soc. Photo-Opt. Instrum. Eng. 2035, pp. 218–229.

Bakushinskiĭ, A. B. (1992). On a convergence problem of the iterative-regularized Gauss-Newton method, *Zh. Vychisl. Mat. i Mat. Fiz.* 32(9): 1503–1509.

Biswal, N. C., Pavlik, C., Smith, M. B., Aguirre, A., Xu, Y., Zanganeh, S., Kuhn, L. T., Claffey, K. P. & Zhu, Q. (2011). Imaging tumor hypoxia by near-infrared fluorescence tomography, *J. Biomed. Opt.* 16(6): 066009.

Blaschke, B., Neubauer, A. & Scherzer, O. (1997). On convergence rates for the iteratively regularized Gauss-Newton method, *IMA J. Numer. Anal.* 17(3): 421–436.

Chance, B., Cope, M., Gratton, E., Ramirez, N. & Tromberg, B. J. (1998). Phase measurement of light absorption and scatter in human tissue, *Rev. Sci. Instr.* 69: 3457 – 3481.

Chaudhari, A. J., Ahn, S., Levenson, R., Badawi, R. D., Cherry, S. R. & Leahy, R. M. (2009). Excitation spectroscopy in multispectral optical fluorescence tomography: methodology, feasibility and computer simulation studies, *Phys. Med. Biol.* 54(15): 4687–4704.

Chaudhari, A. J., Darvas, F., Bading, J. R., Moats, R. A., Conti, P. S., Smith, D. J., Cherry, S. R. & Leahy, R. M. (2005). Hyperspectral and multispectral bioluminescence optical tomography for small animal imaging, *Phys. Med. Biol.* 50(23): 5421–5441.

Chen, Y. Y. & Wood, A. W. (2009). Application of a temperature-dependent fluorescent dye (rhodamine b) to the measurement of radiofrequency radiation-induced temperature changes in biological samples, *Bioelectromagnetics* 30: 583–590.

Corlu, A., Choe, R., Durduran, T., Rosen, M. A., Schweiger, M., Arridge, S. R., Schnall, M. D. & Yodh, A. G. (2007). Three-dimensional in vivo fluorescence diffuse optical tomography of breast cancer in humans, *Opt. Express* 15(11): 6696–6716.

Culver, J. P., Choe, R., Holboke, M. J., Zubkov, L., Durduran, T., Slemp, A., Ntziachristos, V., Chance, B. & Yodh, A. G. (2003). Three-dimensional diffuse optical tomography in the parallel plane transmission geometry: evaluation of a hybrid frequency domain/continuous wave clinical system for breast imaging, *Med. Phys.* 30(2): 235–247.

da Silva, A., Bordy, T., Debourdeau, M., Dinten, J.-M., Peltié, P. & Rizo, P. (2007). Coupling x-ray and optical tomography systems for in vivo examination of small animals, *Conf Proc IEEE Eng Med Biol Soc* 2007: 3335–3338.

Davis, S. C., Dehghani, H., Wang, J., Jiang, S., Pogue, B. W. & Paulsen, K. D. (2007). Image-guided diffuse optical fluorescence tomography implemented with Laplacian-type regularization, *Opt. Express* 15(7): 4066–4082.

Davis, S. C., Pogue, B. W., Springett, R., Leussler, C., Mazurkewitz, P., Tuttle, S. B., Gibbs-Strauss, S. L., Jiang, S. S., Dehghani, H. & Paulsen, K. D. (2008). Magnetic resonance-coupled fluorescence tomography scanner for molecular imaging of tissue, *Rev. Sci. Instrum.* 79(6): 064302.

Dehghani, H., Eames, M. E., Yalavarthy, P. K., Davis, S. C., Srinivasan, S., Carpenter, C. M., Pogue, B. W. & Paulsen, K. D. (2008). Near infrared optical tomography using NIRFAST: Algorithms for numerical model and image reconstruction algorithms, *Commun. Numer. Methods Eng.* 25(6): 711–732.

Douiri, A., Schweiger, M., Riley, J. & Arridge, S. R. (2007). Anisotropic diffusion regularization methods for diffuse optical tomography using edge prior information, *Meas. Sci. Technol.* 18(1): 87–95.

Durduran, T., Choe, R., Baker, W. B. & Yodh, A. G. (2010). Diffuse optics for tissue monitoring and tomography, *Rep. Prog. Phys.* 73: 1 – 43.

Egger, H. & Leittão, A. (2009). Nonlinear regularization methods for ill-posed problems with piecewise constant or strongly varying solutions, *Inv. Probl.* 25: 115014.

Egger, H. & Schlottbom, M. (2011). Efficient reliable image reconstruction schemes for diffuse optical tomography, *Inv. Probl. Sci. Engrg.* 19(2): 155–180.

Engl, H. W., Hanke, M. & Neubauer, A. (1996). *Regularization of Inverse Problems*, Kluwer, Dordrecht.

Fang, Q. & Boas, D. A. (2009). Monte carlo simulation of photon migration in 3d turbid media accelerated by graphics processing units, *Opt. Express* 17(22): 20178–20190.

Frühauf, F., Scherzer, O. & Leitão, A. (2005). Analysis of regularization methods for the solution of ill-posed problems involving discontinuous operators, *SIAM J. Numer. Anal.* 43: 767–786.

Gaind, V., Kularatne, S., Low, P. S. & Webb, K. J. (2010). Deep–tissue imaging of intramolecular fluorescence resonance energy-transfer parameters., *Opt Lett* 35(9): 1314–1316.

Gannot, I., Ron, I., Hekmat, F., Chernomordik, V. & Gandjbakhche, A. (2004). Functional optical detection based on ph dependent fluorescence lifetime, *Lasers Surg. Med.* 35(5): 342–348.

Gibson, A. P., Hebden, J. C. & Arridge, S. R. (2005). Recent advances in diffuse optical imaging, *Phys. Med. Biol.* 50: R1–R43.

Godavarty, A., Eppstein, M. J., Zhang, C., Theru, S., Thompson, A. B., Gurfinkel, M. & Sevick-Muraca, E. M. (2003). Fluorescence-enhanced optical imaging in large tissue volumes using a gain-modulated ICCD camera, *Phys. Med. Biol.* 48: 1701–1720.

Graves, E. E., Ripoll, J., Weissleder, R. & Ntziachristos, V. (2003). A submillimeter resolution fluorescence molecular imaging system for small animal imaging, *Med. Phys.* 30(5): 901–911.

Haller, J., Hyde, D., Deliolanis, N., de Kleine, R., Niedre, M. & Ntziachristos, V. (2008). Visualization of pulmonary inflammation using noninvasive fluorescence molecular imaging, *J. Appl. Physiol.* 104(3): 795–802.

Hanke, M. (1997). Regularizing properties of a truncated Newton-CG algorithm for nonlinear inverse problems, *Numer. Func. Anal. Optim.* 18: 971–993.

Hebden, J. C., Arridge, S. R. & Delpy, D. T. (1997). Optical imaging in medicine: I. experimental techniques, *Phys. Med. Biol.* 42: 825–840.

Hyde, D., Miller, E., Brooks, D. & Ntziachristos, V. (2010). Data specific spatially varying regularization for multimodal fluorescence molecular tomography, *IEEE Trans. Med. Imag.* 29(2): 365–374.

Jiang, H. (1998). Frequency-domain fluorescent diffusion tomography: A finite-element-based algorithm and simulations, *Appl. Opt.* 37: 5337–5343.

Joshi, A., Bangerth, W. & Sevick-Muraca, W. M. (2004). Adaptive finite element based tomography for fluorescence optical imaging in tissue, *Opt. Express* 12: 5402–5417.

Kaltenbacher, B. (1997). Some newton-type methods for the regularization of nonlinear ill-posed problems, *Inv. Probl.* 13: 729–753.

Kepshire, D., Mincu, N., Hutchins, M., Gruber, J., Dehghani, H., Hypnarowski, J., Leblond, F., Khayat, M. & Pogue, B. W. (2009). A microcomputed tomography guided

fluorescence tomography system for small animal molecular imaging, *Rev. Sci. Instrum.* 80(4): 043701.

Klose, A. D. & Pöschinger, T. (2011). Excitation-resolved fluorescence tomography with simplified spherical harmonics equations, *Phys. Med. Biol.* 56(5): 1443–1469.

Kozloff, K. M., Weissleder, R. & Mahmood, U. (2007). Noninvasive optical detection of bone mineral, *J. Bone Miner. Res.* 22(8): 1208–1216.

Kumar, A. T. N., Raymond, S. B., Dunn, A. K., Bacskai, B. J. & Boas, D. A. (2008). A time domain fluorescence tomography system for small animal imaging, *IEEE Trans. Med. Imag.* 27: 1152–1163.

Lakowicz, J. R. (2006). *Priciples of Fluorescence Spectroscopy*, Springer.

Leblond, F., Davis, S. C., Valdés, P. A. & Pogue, B. W. (2010). Pre-clinical whole-body fluorescence imaging: Review of instruments, methods and applications, *J. Photochem. Photobiol. B* 98(1): 77–94.

Li, C., Mitchell, G. S., Dutta, J., Ahn, S., Leahy, R. M. & Cherry, S. R. (2009). A three-dimensional multispectral fluorescence optical tomography imaging system for small animals based on a conical mirror design, *Opt. Express* 17(9): 7571–7585.

Li, D. U., Arlt, J., Richardson, J., Walker, R., Buts, A., Stoppa, D., Charbon, E. & Henderson, R. (2010). Real–time fluorescence lifetime imaging system with a 32x32 0.13um cmos low dark–count single-photon avalanche diode array, *Opt. Express* 18: 10257?–10269.

Lin, Y., Barber, W. C., Iwanczyk, J. S., Roeck, W., Nalcioglu, O. & Gulsen, G. (2010). Quantitative fluorescence tomography using a combined tri-modality ft/dot/xct system, *Opt. Express* 18(8): 7835–7850.

Longmuir, I. S. & Knopp, J. A. (1976). Measurement of tissue oxygen with a fluorescent probe, *J. Appl. Physiol.* 41(4): 598–602.

Marquardt, D. (1963). An algorithm for least-squares estimation of nonlinear parameters, *SIAM J. Appl. Math.* 11: 431–441.

Masciotti, J. M., Lee, J., Hielscher, A. H. & Stewart, M. (2009). Instrumentation for simultaneous magnetic resonance and optical tomographic imaging of the rodent brain, *Proc. SPIE 7171*.

Mastanduno, M. A., Davis, S. C., Jiang, S., diFlorio Alexander, R., Pogue, B. W. & Paulsen, K. D. (2011). Combined three–dimensional magnetic resonance guided optical spectroscopy for functional and molecular imaging of human breast cancer, *Proc. of SPIE-OSA Biomedical Optics, SPIE Vol. 8089*.

McGinty, J., Stuckey, D. W., Soloviev, V. Y., Laine, R., Wylezinska-Arridge, M., Wells, D. J., Arridge, S. R., French, P. M. W., Hajnal, J. V. & Sardini, A. (2011). In vivo fluorescence lifetime tomography of a FRET probe expressed in mouse, *Biomed. Opt. Express* 2(7): 1907–1917.

Mordon, S., Maunoury, V., Devoisselle, J. M., Abbas, Y. & Coustaud, D. (1992). Characterization of tumorous and normal tissue using a ph-sensitive fluorescence indicator (5,6-carboxyfluorescein) in vivo, *J. Photochem. Photobiol. B* 13(3-4): 307–314.

Morozov, V. A. (1966). On the solution of functional equations by the method of regularization, *Soviet Math. Dokl.* 7: 414–417.

Niclass, C., Rochas, A., Besse, P.-A. & Charbon, E. (2004). Toward a 3-D camera based on single photon avalanche diodes, *IEEE J. Sel. Topics Quant. Electr.* 10: 796 – 802.

Niedre, M. J., de Kleine, R. H., Aikawa, E., Kirsch, D. G., Weissleder, R. & Ntziachristos, V. (2008). Early photon tomography allows fluorescence detection of lung

carcinomas and disease progression in mice in vivo, *Proc Natl Acad Sci U S A* 105(49): 19126–19131.

Nissilä, I., Hebden, J. C., Jennions, D., Heino, J., Schweiger, M., Kotilahti, K., Noponen, T., Gibson, A., Järvenpää, S., Lipiäinen, L. & Katila, T. (2006). Comparison between a time-domain and a frequency-domain system for optical tomography, *J. Biomed. Opt.* 11(6): 064015.

Nissilä, I., Noponen, T., Kotilahti, K., Katila, T., Lipiäinen, L., Tarvainen, T., Schweiger, M. & Arridge, S. (2005). Instrumentation and calibration methods for the multichannel measurement of phase and amplitude in optical tomography, *Rev. Sci. Instrum.* 76: 04432–1–04432–10.

Nothdurft, R. E., Patwardhan, S. V., Akers, W., Ye, Y., Achilefu, S. & Culver, J. P. (2009). In vivo fluorescence lifetime tomography, *J. Biomed. Opt.* 14(2): 024004–1–7.

Ntziachristos, V., Yodh, A., Schnall, M. & Chance, B. (2000). Concurrent MRI and diffuse optical tomography of breast after indocyanine green enhancement, *Proc. Natl. Acad. Sci.* 97: 2767–2772.

Panagiotou, C., Somayajula, S., Gibson, A. P., Schweiger, M., Leahy, R. M. & Arridge, S. R. (2009). Information theoretic regularization in diffuse optical tomography, *JOSA A* 26: 1277–1290.

Patwardhan, S. V. & Culver, J. P. (2008). Quantitative diffuse optical tomography for small animals using an ultrafast gated image intensifier, *J. Biomed. Opt.* 13(1): 011009.

Pavia, J. M., Charbon, E. & Wolf, M. (2011). 3d near-infrared imaging based on a singlephoton avalanche diode array sensor, *Proc. SPIE 8088, 808811*.

Reynolds, J. S., Troy, T. L. & Sevick-Muraca, E. M. (1997). Multipixel techniques for frequency-domain photon migration imaging, *Biotechnol. Prog.* 13: 669–690.

Roy, R. & Sevick-Muraca, E. M. (1999). Truncated Newton's optimization scheme for absorption and fluorescence optical tomography: Part I theory and formulation, *Opt. Express* 4: 353–371.

Schmidt, F., Fry, M., E.M.C.Hillman, Hebden, J. & Delpy, D. (2000). A 32 channel time-resolved instrument for medical optical tomography, *Rev. Sci. Instrum.* 71: 256–265.

Schulz, R. B., Ale, A., Sarantopoulos, A., Freyer, M., Soehngen, E., Zientkowska, M. & Ntziachristos, V. (2010). Hybrid system for simultaneous fluorescence and x-ray computed tomography, *IEEE Trans. Med. Imag.* 29(2): 465–473.

Schulz, R. B., Ripoll, J. & Ntziachristos, V. (2004). Experimental fluorescence tomography of tissues with noncontact measurements, *IEEE Trans. Med. Imag.* 23(4): 492–500.

Schweiger, M., Arridge, S. R. & Nissilä, I. (2005). Gauss–Newton method of image reconstruction in diffuse optical tomography, *Phys. Med. Biol.* 50: 2365–2386.

Schweiger, M., Dorn, O. & Arridge, S. R. (2008). 3-D shape and contrast reconstruction in optical tomography with level sets, *Journal of Physics: Conference Series* 124(1): 012043.

Sevick, E. M. & Chance, B. (1991). Photon migration in a model of the head measured using time and frequency domain techniques: potentials of spectroscopy and imaging, *in* B. Chance & A. Katzir (eds), *Time-Resolved Spectroscopy and Imaging of Tissues*, Proc. Soc. Photo-Opt. Instrum. Eng. 1431, pp. 84–96.

Sevick-Muraca, E. M., Kuwana, E., Godavarty, A., Houston, J. P., Thompson, A. B. & Roy, R. (2003). Near-infrared fluorescence imaging and spectroscopy in random media and tissue, *in* T. Vo-Dinh (ed.), *Biomedical Photonics Handbook*, CRC Press, Boca Raton, chapter 33.

Sevick-Muraca, E. M. & Rasmussen, J. C. (2008). Molecular imaging with optics: primer and case for near-infrared fluorescence techniques in personalized medicine, *J. Biomed. Opt.* 13(4): 041303.

Shives, E., Xu, Y. & Jiang, H. (2002). Fluorescence lifetime tomography of turbid media based on an oxygen-sensitive dye, *Opt. Express* 10: 1557–1562.

Silva, A. D., Leabad, M., Driol, C., Bordy, T., Debourdeau, M., Dinten, J.-M., Peltié, P. & Rizo, P. (2009). Optical calibration protocol for an x-ray and optical multimodality tomography system dedicated to small-animal examination, *Appl. Opt.* 48(10): D151–D162.

Soloviev, V. Y., D'Andrea, C., Valentini, G., Cubeddu, R. & Arridge, S. R. (2009). Combined reconstruction of fluorescent and optical parameters using time-resolved data, *Appl. Opt.* 48(1): 28–36.

Sosnovik, D. E., Nahrendorf, M., Deliolanis, N., Novikov, M., Aikawa, E., Josephson, L., Rosenzweig, A., Weissleder, R. & Ntziachristos, V. (2007). Fluorescence tomography and magnetic resonance imaging of myocardial macrophage infiltration in infarcted myocardium in vivo, *Circulation* 115(11): 1384–1391.

Tan, Y., Novo, M., Yao, L., Zhou, L. & Jiang, H. (n.d.). In vivo monitoring of stem cells in drosophila pupae using the radiative transfer equation-based fluorescence molecular tomography, *Mol. Imag. Biol.* pp. 1–6. 10.1007/s11307-010-0434-6.

Wang, D., Liu, X., Liu, F. & Bai, J. (2010). Full-angle fluorescence diffuse optical tomography with spatially coded parallel excitation, *IEEE Trans Inf Technol Biomed* 14(6): 1346–1354.

Wang, L.-H., Jacques, S. L. & Zheng, L.-Q. (1995). MCML - monte carlo modeling of photon transport in multi-layered tissues, *Computer Methods and Programs in Biomedicine* 47: 131–146.

Yang, X., Gong, H., Quan, G., Deng, Y. & Luo, Q. (2010). Combined system of fluorescence diffuse optical tomography and microcomputed tomography for small animal imaging, *Rev. Sci. Instrum.* 81(5): 054304.

Zacharakis, G., Favicchio, R., Simantiraki, M. & Ripoll, J. (2011). Spectroscopic detection improves multi-color quantification in fluorescence tomography, *Biomed. Opt. Express* 2(3): 431–439.

Zavattini, G., Vecchi, S., Mitchell, G., Weisser, U., Leahy, R. M., Pichler, B. J., Smith, D. J. & Cherry, S. R. (2006). A hyperspectral fluorescence system for 3d in vivo optical imaging, *Phys. Med. Biol.* 51(8): 2029–2043.

Zhang, X. & Badea, C. (2009). Effects of sampling strategy on image quality in noncontact panoramic fluorescence diffuse optical tomography for small animal imaging, *Opt. Express* 17(7): 5125–5138.

Zhang, X. & Badea, C. T. (2011). Highly efficient detection in fluorescence tomography of quantum dots using time-gated acquisition and ultrafast pulsed laser, *Proc Soc Photo Opt Instrum Eng* p. 7896.

Zhang, X., Badea, C. T. & Johnson, G. A. (2009). Three-dimensional reconstruction in free-space whole-body fluorescence tomography of mice using optically reconstructed surface and atlas anatomy, *J. Biomed. Opt.* 14(6): 064010.

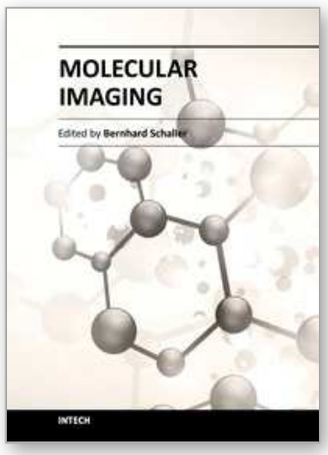

Molecular Imaging

Edited by Prof. Bernhard Schaller

ISBN 978-953-51-0359-2
Hard cover, 390 pages
Publisher InTech
Published online 16, March, 2012
Published in print edition March, 2012

The present book gives an exceptional overview of molecular imaging. Practical approach represents the red thread through the whole book, covering at the same time detailed background information that goes very deep into molecular as well as cellular level. Ideas how molecular imaging will develop in the near future present a special delicacy. This should be of special interest as the contributors are members of leading research groups from all over the world.

How to reference

In order to correctly reference this scholarly work, feel free to copy and paste the following:

Manuel Freiberger and Hermann Scharfetter (2012). 3D Optical Imaging of Fluorescent Agents in Biological Tissues, Molecular Imaging, Prof. Bernhard Schaller (Ed.), ISBN: 978-953-51-0359-2, InTech, Available from: http://www.intechopen.com/books/molecular-imaging/3d-optical-imaging-of-fluorescent-agents-in-biological-tissues

INTECH
open science | open minds

InTech Europe
University Campus STeP Ri
Slavka Krautzeka 83/A
51000 Rijeka, Croatia
Phone: +385 (51) 770 447
Fax: +385 (51) 686 166
www.intechopen.com

InTech China
Unit 405, Office Block, Hotel Equatorial Shanghai
No.65, Yan An Road (West), Shanghai, 200040, China
中国上海市延安西路65号上海国际贵都大饭店办公楼405单元
Phone: +86-21-62489820
Fax: +86-21-62489821

IntechOpen